

# **Enhanced energy absorption performance of 3D printed 2D auxetic lattices**

Niranjan Kumar Choudhry<sup>1</sup>, Biranchi Panda<sup>1\*</sup>, S. Kumar<sup>2,3\*</sup>

<sup>1</sup>Sustainable Resources for Additive Manufacturing (SreAM) Lab, Department of Mechanical Engineering, Indian Institute of Technology Guwahati, India

<sup>2</sup>James Watt School of Engineering, University of Glasgow, Glasgow G12 8QQ, UK

<sup>3</sup>Glasgow Computational Engineering Centre, University of Glasgow, Glasgow G12 8LT, UK

## Supplementary Information

### **S1: Experimental setup for quasi-static compression test**

Fig. S1 shows the experimental setup used for the quasi-static compression test. The components of 250 kN UTM (MEDIAN 250) are highlighted in fig. S1. The top platen is connected to the load cell which is mounted on a crosshead. The crosshead is mounted on the column, and its position is fixed before the start of a compression test. Here top platen is fixed and movement is given to the bottom platen. The compression test is performed at room temperature and recorded using Sony NXCAM Video Camera. For any emergency condition, the emergency stop button can be used.

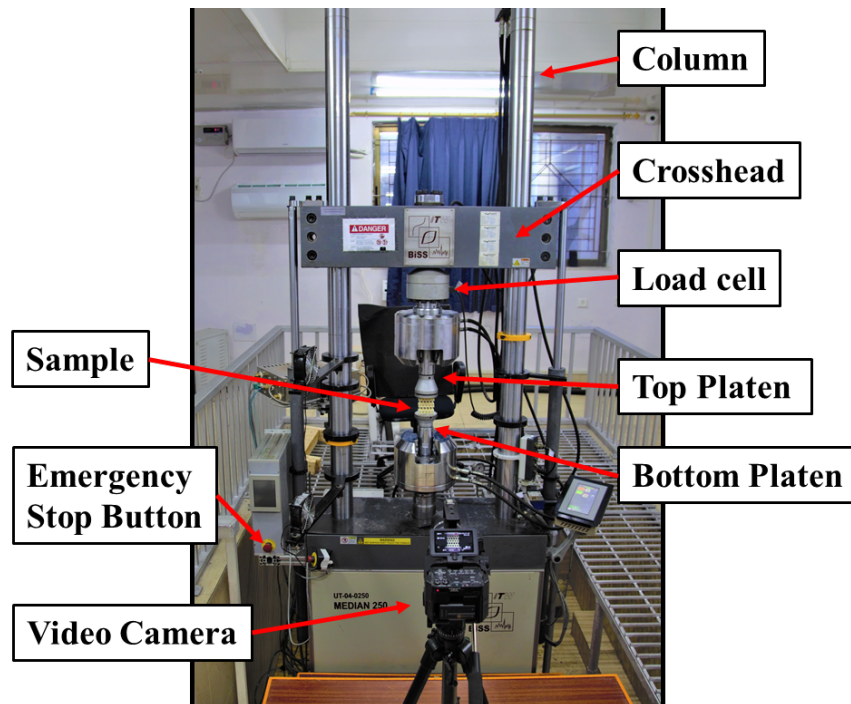


**Fig. S1** Experimental setup for quasi-static compression test

### **S2: Material characterization**

**(a) Tensile response:-** Uniaxial tensile test was performed on three identical dogbone samples using a 5kN load cell Zwick-Roell UTM. The gauge length of the dogbone sample is 25mm, and its width and thickness is 6mm and 2mm respectively. The dogbone samples were fabricated by FDM 3D printing (printing parameters are given in section 3.1) with ABS polymer. Samples were placed in the grip of the UTM and the tensile load was applied with a

crosshead speed of 2mm/min till samples failed. The engineering stress-strain response of specimens was calculated from load-displacement data. The engineering stress-strain response of 3D printed dogbone sample during tension was presented in fig.S2.

**(b) Compressive response of ABS material:-** Three identical cuboidal samples having an edge length of 12.7mm and a height of 25.4mm were fabricated by the FDM 3D printing (printing parameters are given in section 3.1) with ABS polymer. A quasi-static compression test was performed with 250 kN UTM (MEDIAN 250) at the crosshead speed of 2 mm/min. The samples were loaded in between the top and bottom platens. Crushing forces were recorded through a 250 kN load cell. The engineering stress-strain response of 3D printed cuboidal sample during compression was presented in fig.S2.

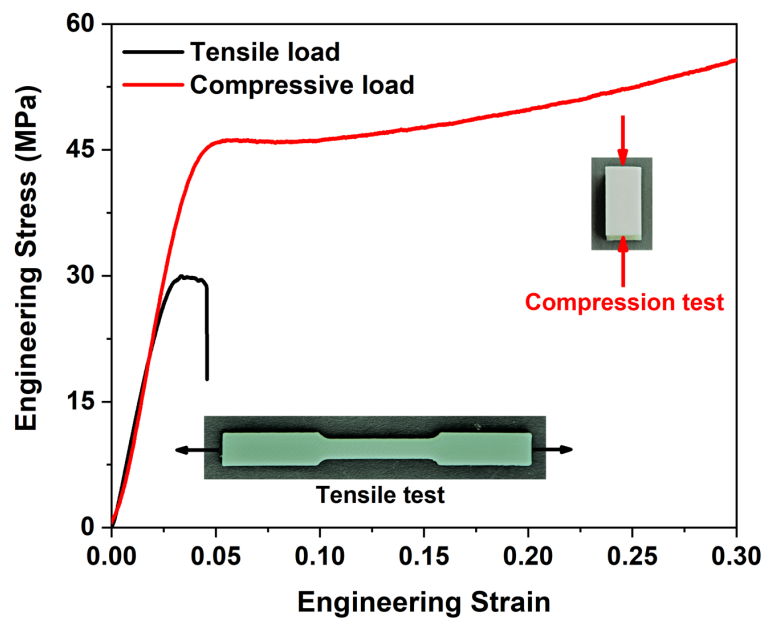


**Fig. S2** Engineering stress-strain response of FDM printed specimens.

Elastic properties of base material is given in table S1 which is derived from the engineering stress-strain response of FDM printed specimens.

**Table S1** Elastic properties of 3D printed ABS specimen.

Material	Elastic modulus (MPa)	Yield stress (MPa)	Poisson's ratio	Density (g/cm <sup>3</sup> )
ABS	2000	29	0.35	1.05

### S3: FEA model and its constitutive description

For systematically analyzing the quasi-static compression response of 3D printed auxetic structures, FE analysis was conducted using a commercial FE package (ABAQUS) with a nonlinear explicit solver. ABS polymer exhibited significantly different yield behavior in tension and compression as can be seen in fig. S2, and hence a pressure-dependent plasticity model was used to model the material behavior. Isotropic elasticity was considered for modeling the elastic behavior of ABS polymer while plastic behavior was modeled by using the Linear Drucker-Prager plasticity model. The Ductile Damage Model was considered for modeling material failure. The input parameters required for the Linear Drucker-Prager plasticity model and Ductile Damage Model are given in table S2 and table S3 respectively.

The model decomposes the total strain rate into two parts one is elastic strain rate while the other is plastic strain rate as given below

$$\dot{\epsilon} = \dot{\epsilon}^e + \dot{\epsilon}^p \quad (S1)$$

Where  $\dot{\epsilon}$  is the total strain rate while  $\dot{\epsilon}^e$  and  $\dot{\epsilon}^p$  are the elastic and plastic components of the total strain rate respectively. The stress-strain relationship by employing scalar damage elasticity can be written as

$$\sigma = D^e : (\epsilon - \epsilon^p) \quad (S2)$$

where  $D^e$  is degraded elastic stiffness tensor which relates with undegraded elastic stiffness  $D_0^e$  as

$$D^e = (1 - d)D_0^e \quad (S3)$$

$d$  is known as a scalar elastic damage variable having a value between 0 and 1. When  $d = 0$ , it means the material is undamaged while at  $D = 1$ , the material is completely ruptured ( the load-carrying capacity of material has been lost). Considering the degradation of the material is due to the growth of microcracks and voids, and hence having reduced resistance area. So the effective stress can be represented as

$$\bar{\sigma} = \frac{\sigma}{(1-d)} = D_0^e : (\epsilon - \epsilon^p) \quad (S4)$$

Which is used for formulating the plasticity behavior.

Yield surface evolution is controlled by employing isotropic hardening variables in the form of equivalent plastic strains for both tension ( $\tilde{\epsilon}_t^p$ ) and compression ( $\tilde{\epsilon}_c^p$ ), and can be given as (in rate form)

$$\dot{\tilde{\epsilon}}^p = \mathbf{h}(\bar{\sigma}, \tilde{\epsilon}^p) \cdot \dot{\epsilon}^p \quad (\text{S5})$$

Where

$$\tilde{\epsilon}^p = \begin{bmatrix} \tilde{\epsilon}_t^p \\ \tilde{\epsilon}_c^p \end{bmatrix} \quad (\text{S6})$$

The yield function for the Drucker-Prager model is written as

$$F(\bar{\sigma}, \tilde{\epsilon}^p) \leq 0 \quad (\text{S7})$$

The non-associated flow rule can be given as

$$\dot{\epsilon}^p = \dot{\lambda} \frac{\partial G(\bar{\sigma})}{\partial \bar{\sigma}} \quad (\text{S8})$$

where  $\dot{\lambda}$  and  $\frac{\partial G(\bar{\sigma})}{\partial \bar{\sigma}}$  are the non-negative plastic multiplier and the normal vector to the plastic flow potential surface  $G(\bar{\sigma})$  respectively.

**Table S2** Linear Drucker-Prager plasticity parameters with Isotropic hardening in uniaxial tension for ABS polymer.

Angle of Friction ( $\beta$ )	Flow Stress Ratio	Dilation Angle ( $\psi$ )
12°	0.8216	12°

**Table S3** Ductile Damage Model parameters for ABS polymer.

Fracture Strain	Stress Triaxiality	Strain Rate (1/s)	Fracture Energy (N/mm)
0.625	- 0.33	0.00133	0.27
0.008	0.33	0.00133	0.27

#### S4: Mesh convergence test

Fig.S3 represents a mesh convergence study where both the elastic and plastic behavior of the re-entrant honeycomb (RH) structure was considered. A load-displacement curve is drawn for different mesh element sizes. For a coarser mesh size, the prediction of structural performance was not appropriate, but as mesh element size is refined or reduced, the accuracy of results

increases and becomes stable. For both the mesh element size i.e. 0.25mm & 0.20mm the results predicted is the same, and hence a mesh size of 0.25mm is used for finding the FE results.

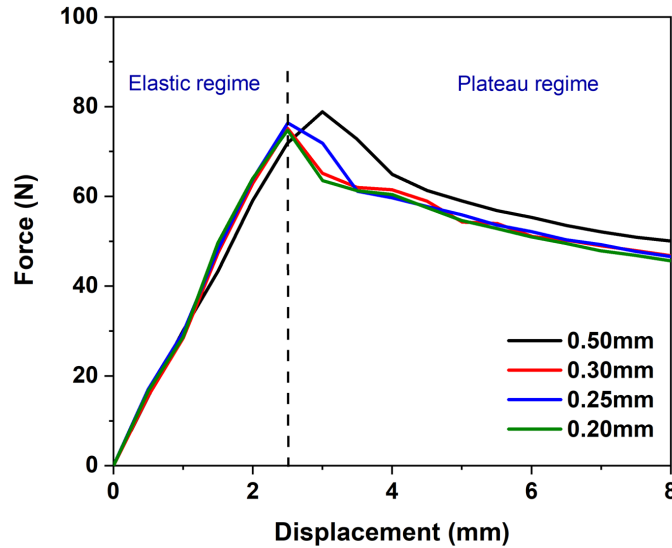


**Fig. S3** Prediction of FE results for various mesh density.

### **S5: Optical microscope imaging of FDM printed structures**

Optical images were taken from an optical microscope with a 10x magnification at different locations of the FDM printed part. Voids with different sizes were found at different cross-sections as shown in fig. S4. It was observed that the vertical strut at some locations within the structures delaminated with an average gap of 0.2355 mm, while at some joints, material was partially filled leading to the formation of voids up to 0.571mm × 0.649mm. At the joints, the cross-section area is more than the ligaments, requiring more material to fill.

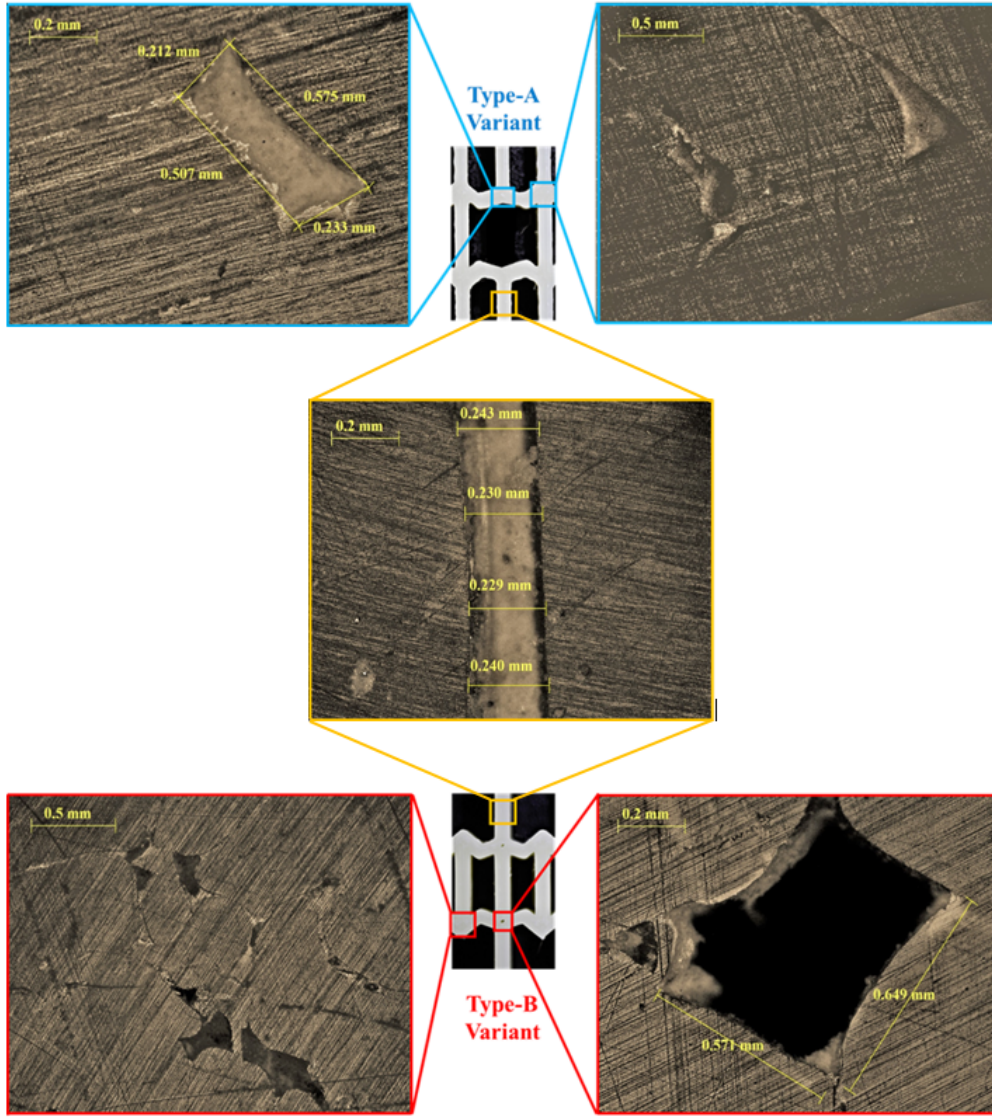


**Fig. S4** Optical images of FDM printed parts at different cross-sections.

### **S6: Sub cell analysis of Type A and B structures**

The new type-A and B variant lattice structures are resulted due to addition of vertical ligament, which produces composite structures with different sub-cell properties (see fig. S5). The stiffness of these sub-cells can be compared and analyzed through Maxwell's stability factor ( $M$ ) which highlights deformation mode of the sub-cells ( $M \geq 0$ , stretching dominated or  $M < 0$ , bending dominated). For all cases, the Maxwell's stability factor ( $M$ ) is less than zero and hence it has bending dominated deformation mode.

The overall stiffness of the composite structures can be determined through the rule of mixture [32]. For this purpose, sub cell properties of Type A and B structures are first calculated theoretically, and thereafter the rule of mixture has been used to get the upper and lower bound of Young's modulus. It is important to note that the sub-cells should be homogeneously dispersed throughout the structure. Fig. S5 shows the different sub-cells present within these structures.

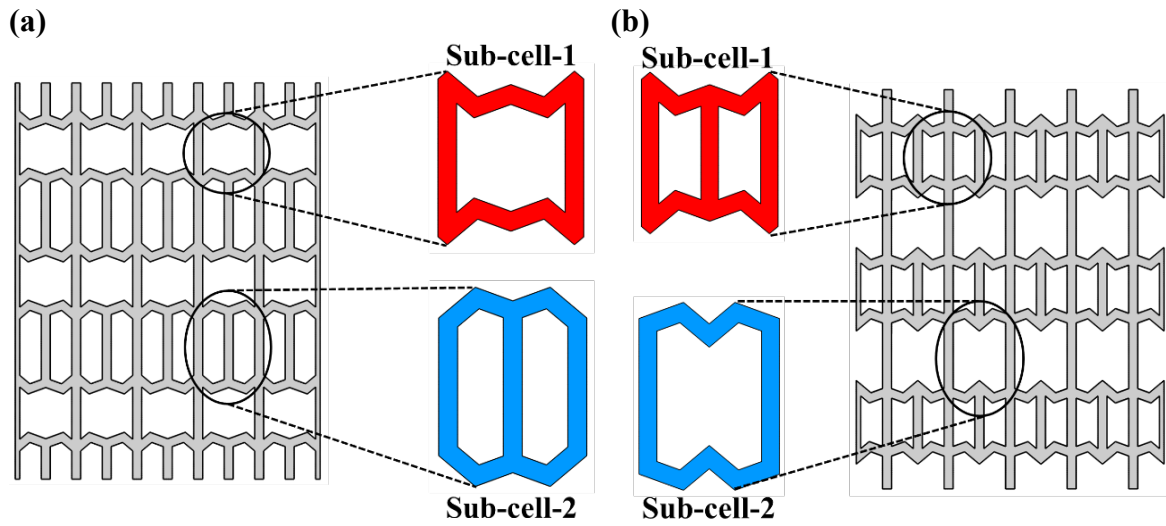


**Fig. S5** Semi- regular binary edge to edge tessellation of structures highlighted with their sub cell (a) Type-A variant and (b) Type-B variant.

The ‘rule of mixture’ for composite material was used to estimate the Young's modulus of Type A and B structures. The expressions used for the upper (equation-S9) and lower bound (equation-S10) of Young's modulus are as follows [34].

$$E(u) = E_A V_A + E_B V_B \quad (\text{S9})$$

$$E(l) = \frac{E_A E_B}{E_A V_B + E_B V_A} \quad (\text{S10})$$

Where  $E(u)$  and  $E(l)$  represent the upper and lower bound of Young's modulus for composite material respectively.  $V_A$  and  $V_B$  represent the volume fraction and  $E_A$  and  $E_B$  represent Young's modulus of constituent elements “A & B” respectively. Table S4 shows the properties of sub-cells, calculated using theoretical expression for stiffness (see section 2.2).



It was observed that for Type-A variant, sub cell 1 and 2 have Young's modulus of 437.24 MPa and 329.79 MPa, while Type-B have 464.38 MPa and 193.19 MPa respectively. Since these sub-cells have different volume fractions, mixture rule was applied to predict the final Young's modulus of Type A and B structures. The results are summarized in Table S5. It is clear from the results that the difference in Young's modulus of Type – A and B structures was mainly due to different sub cell properties and it's corresponding volume fractions.

**Table S4** Properties of sub-cells derived theoretically ( $\bar{\rho}_{Ai}$  and  $\bar{\rho}_{Bi}$  are the relative density of ith sub cell of Type A and B structures respectively)

Sub-cell	Type-A variant			Type-B variant	
	$V_i$	$E_{Ai}$ (MPa)	$\bar{\rho}_{Ai}$	$E_{Bi}$ (MPa)	$\bar{\rho}_{Bi}$
Sub-cell-1	0.47	437.24	0.37	464.38	0.46
Sub-cell-2	0.53	329.79	0.33	193.19	0.25

**Table S5** Comparison of theoretical result of stiffness with “rule of mixture” prediction

Structure	Young's modulus (MPa)		
	$E(u)$	$E(l)$	Theoretical
Type-A Variant	380.2915	372.8549901	379.74
Type-B Variant	320.6493	266.275038	272.59

Similarly, the difference in sub-cell properties can affect the energy absorption behavior of Type A and B structures. As shown in fig. S6(a) there was a linear increase in stress, as both sub-cells of the structure deformed uniformly and elastically due to the instant stress distribution throughout the unit cell. This linear deformation continued till the unit cell is unstable, and stress drop was observed due to the collapse of the lower relative density sub-cell. After the yield point (end of the elastic regime), sub-cell-1 started deforming due to the buckling of vertical walls and continued till it completely deformed (up to  $\epsilon = 0.286$ ). Further compression causes rotation of the inclined strut about the lower node connecting joint which improves the stability of the unit cell, leading to a rise in stress value (up to  $\epsilon = 0.317$ ). Thereafter deformation of sub-cell-2 started and it collapsed due to bending. Finally, densification of the collapsed layer started as the lower node connecting joint allowed further rotation of the inclined strut, thus resulting denser deformed layer before the onset of densification (fig. S6(a)).

On the other hand, sub-cell 2 of the Type B structure has a lower relative density than subcell-1. From fig. S6(b) it is clear that after the yield point, sub-cell 2 started deforming due to the buckling of vertical walls and continued till complete collapse of the subcell (up to  $\epsilon = 0.135$ ). Further deformation causes rotation of sub-cell-1 about the joint which improves the stability of the unit cell, leading to increase in stress value (up to  $\epsilon = 0.175$ ). Thereafter deformation of sub-cell-1 started, where the sub-cell collapsed due to rotation and bending. It is clear from the unit cell deformation that after 0.2 strain, there is an abrupt increase in energy absorption of the structure due to the deformation of higher relative density sub-cells, thus improving the overall energy absorption of the lattice structure.

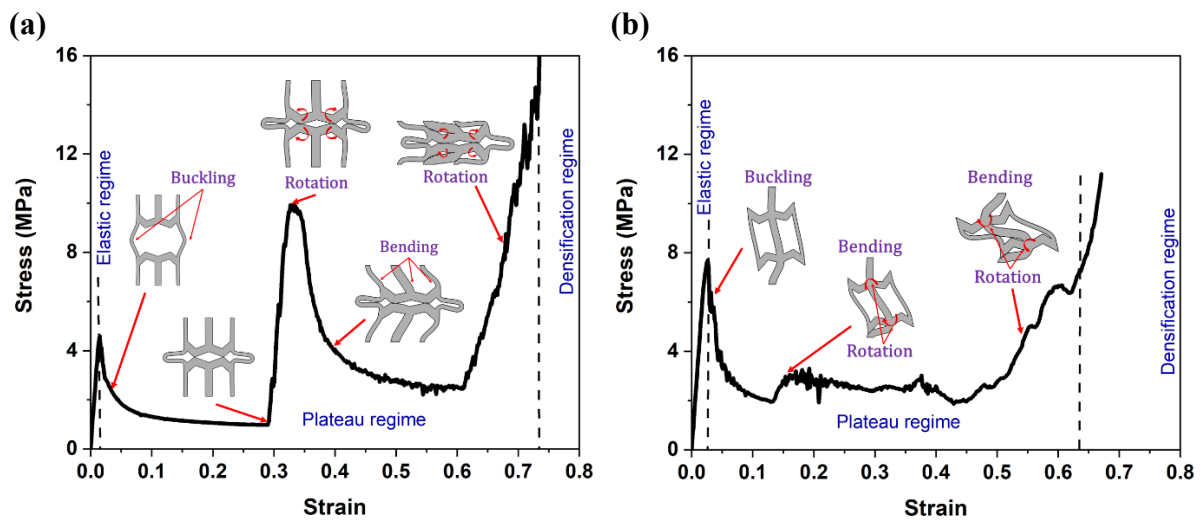


**Fig. S6** Influence of sub-cell sequential deformation on the performance of the unit cell under quasi-static compression; (a). Type-A variant and (b). Type-B variant.

Please note that these deformation modes are observed only with one unit cell in the model whereas the experiment and rest of the simulations were conducted for “m x n” number of cells because the number of cells are chosen such that we avoid the edge effect as detailed in the supplementary information S8.

### **S7: Calculation of geometric constant of proportionality $C$ and exponent “ $n$ ” for the Type-A variant and Type-B variants**

The equation-(S11) shown below is used to understand the scaling relation between Young’s modulus and the relative density for Type-A and Type-B variants.

$$\frac{E}{E_s} = C \left( \frac{\rho^*}{\rho} \right)^n \quad (S11)$$

Where  $E$  and  $E_s$  are Young's modulus of cellular structure and its base material respectively, and  $\rho^*$  and  $\rho$  are the densities of cellular structure and its base material respectively while  $C$  and  $n$  are the geometric constants of proportionality and exponent respectively.

To get the value of “ $C$  and  $n$ ” five data points were generated for each variant (Type-A and Type-B Variant ) and Ln plots between relative Young's modulus and relative density are plotted (fig. S7). Curves were fitted with ‘linear fit’ and ‘intercept and slopes’ of the curves are found which was further used to find the value of “ $C$  and  $n$ ”.

For getting the five data points of each variant (Type-A and Type-B Variant ), the thickness of struts was varied from 1mm to 3mm in a step of 0.5mm while keeping all geometrical parameters constant. The FEA model was used to analyze, and numerical results were used to calculate the relative Young's modulus and relative densities for each setting.

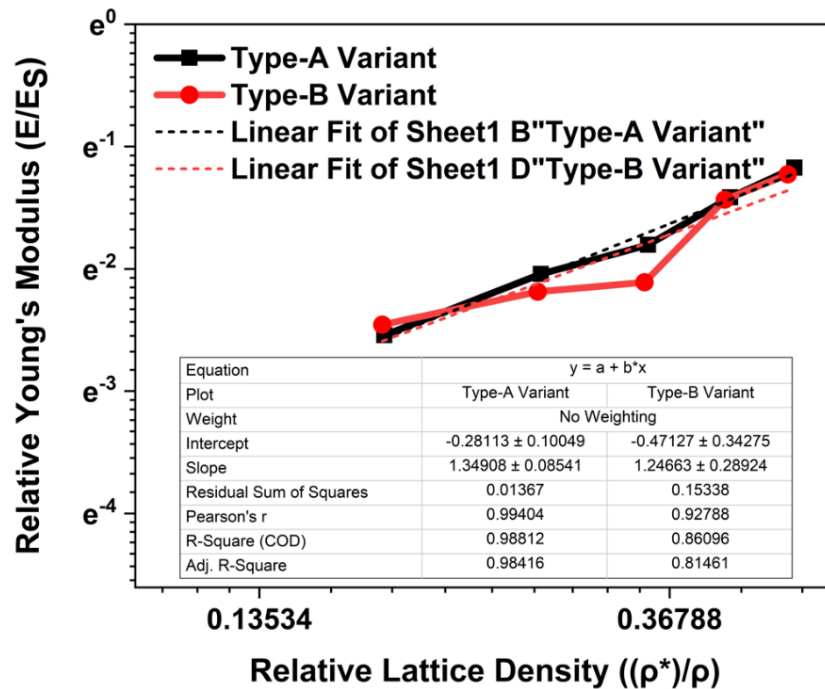


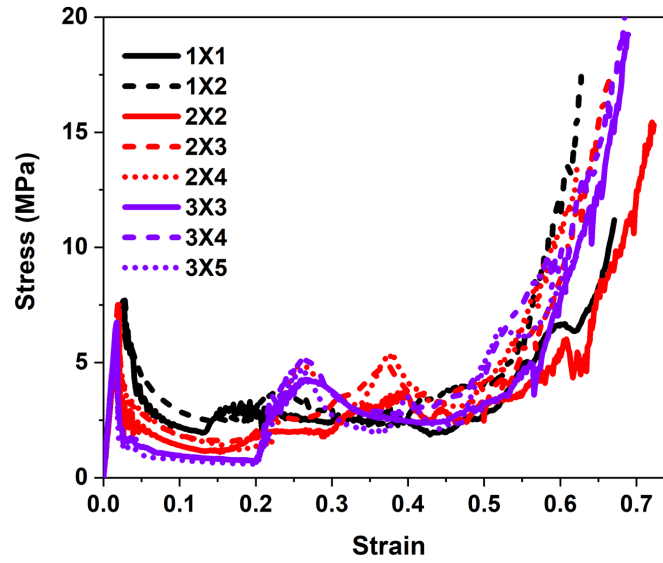
**Fig. S7** Ln plot between relative Young's modulus and relative lattice density of Type A and B Variants

### **S8: Edge effect on the mechanical response, and selection of the appropriate no. of unit cells in rows and columns**

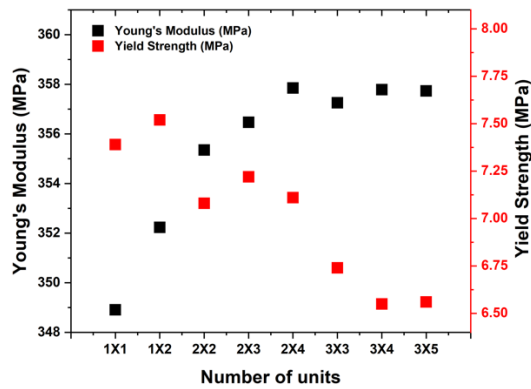
In order to study the effect of no. of unit cells on the mechanical response of the structures, a series of numerical simulations were conducted on “ $m \times n$ ” unit cells structures, where ‘ $m$ ’ and

‘n’ represents the number of unit cells in the row and column respectively. Fig. S8(a) represents the stress-strain response of “m x n” unit cells structure during compression. A more stable plateau region was observed with a single layer of structure and its stability decreased with an increase in the number of layers. It was noted that in a single-layered structure, the stress was uniformly distributed over the load-bearing members (Table S6- 1x1) which leads to a stable plateau region while in the multi-stacked structure, the stress distribution over the load-bearing members was uneven. It is clear from table S6 that the deformation sequences at different strains differ due to changes in the number of layers as the number of layers affects the unit cell's boundary conditions. As compression continued, in the multi-stacked structure there was a random change in a load-bearing position (not found in a single-layered structure) which leads to stress fluctuations within the plateau region (Table S6- 2x2, 3x3). In addition, it is also found that there is a small improvement in densification strain due to an increase in layers within the structure. It is also noted that as more unit cells increased in a layer its average plateau stress increased with a decrease in densification strain.

(a)



(b)



(c)

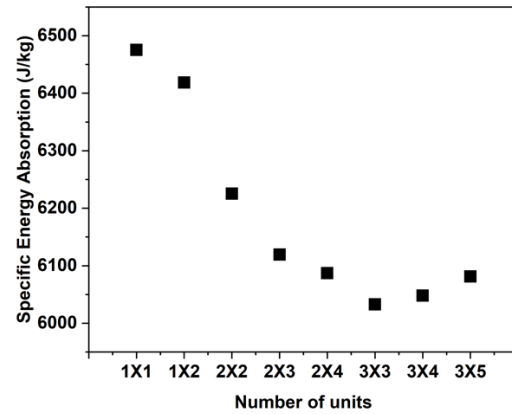
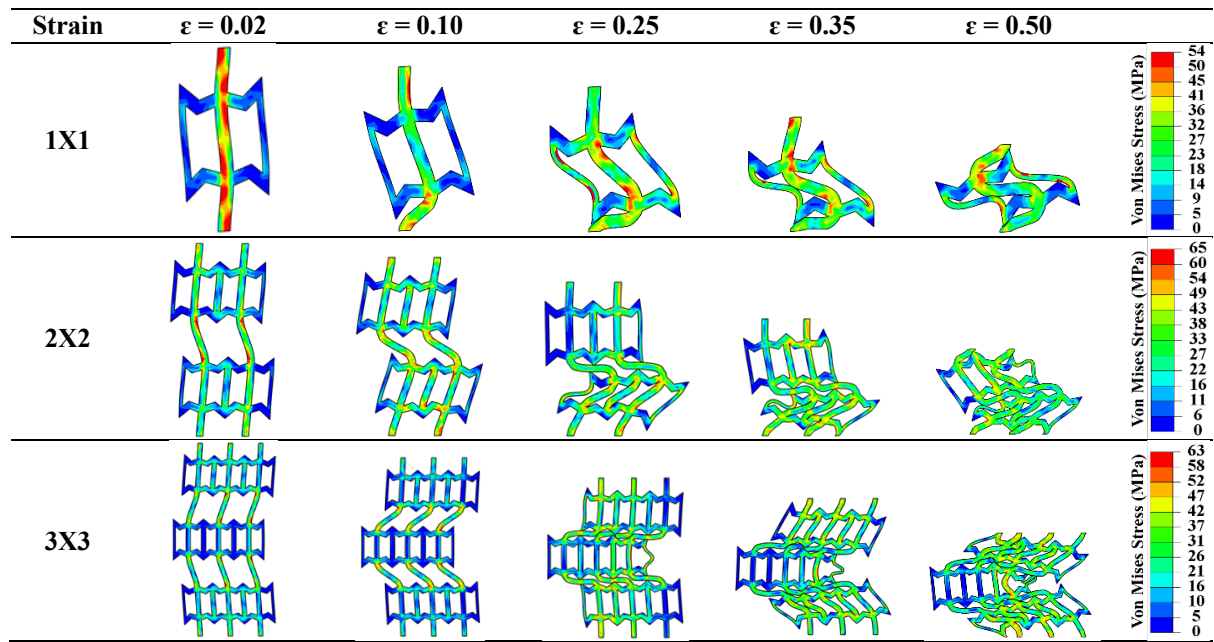


**Fig. S8** Finite element modeling of Type-B variant lattices (a) stress-strain plots of all combinations of unit cells (b) Young's modulus and yield strength vs no. of unit cells plot and (c) specific energy absorption vs no. of unit cells plot

**Table S6** Deformation sequences of “m x n” lattice structures with Von Mises stress distribution diagram.



It is noted that the elastic modulus increased quadratically as the no. of layers increased while yield strength reduced linearly with an increase in the no. of layers. The constraints applied at boundaries in the single-layered structure to large extent restricted movement perpendicular to loading direction and hence high yield strength while as the number of layers increased in the structures the effect of boundary constraints is not experienced by the intermediate layer and hence reduced yield strength. Further, as more unit cells were added in a layer, the fluctuation in Young's modulus and yield strength reduced and became stable after the third layer (fig. S8(b)).

The specific energy absorption (SEA) of a structure is highly affected due to the edge effect. It can be seen from fig. S8(c) that the structure having only one-unit cell showed the highest SEA (6475.45 J/kg), and SEA of the structure value decreased when more no. of unit cells were added, and finally, after adding more than 8 unit cells it becomes stable. For a single unit cell structure, both sides of the unit cell are free, and hence when compression continued they freely rotated about the center (table-4,  $\varepsilon$  at 0.35 & 0.5) and showed higher densification strain due to well-known edge effects. As more no. of unit cells were added in a row, the rotational movement of the structure was restricted and hence earlier densification occurred which can be supported by the stress-strain curve (fig. S8(a)).

